

RESEARCH ARTICLES

6. K. D. Powell, M. E. Goldberg, *J. Neurophysiol.* **84**, 301 (2000).
7. M. A. Steinmetz, C. E. Connor, C. Constantinidis, J. R. McLaughlin, *J. Neurophysiol.* **72**, 1020 (1994).
8. S. Yantis, J. Jonides, *J. Exp. Psychol. Hum. Percept. Perform.* **10**, 601 (1984).
9. H. E. Egeth, S. Yantis, *Annu. Rev. Psychol.* **48**, 269 (1997).
10. M. E. Goldberg, R. H. Wurtz, *J. Neurophysiol.* **35**, 560 (1972).
11. M. I. Posner, *Q. J. Exp. Psychol.* **32**, 3 (1980).
12. E. M. Bowman, V. J. Brown, C. Kertzman, U. Schwarz, D. L. Robinson, *J. Neurophysiol.* **70**, 431 (1993).
13. E. A. Witte, M. Villareal, R. T. Marrocco, *Behav. Brain Res.* **82**, 103 (1996).
14. H. S. Bashinski, V. R. Bacharach, *Percept. Psychophys.* **28**, 241 (1980).
15. V. M. Ciaramitaro, E. L. Cameron, P. W. Glimcher, *Vision Res.* **41**, 57 (2001).
16. T. Moore, M. Fallah, *Proc. Natl. Acad. Sci. U.S.A.* **98**, 1273 (2001).
17. E. Kowler, E. Anderson, B. Doshier, E. Blaser, *Vision Res.* **35**, 1897 (1995).
18. H. Deubel, W. X. Schneider, *Vision Res.* **36**, 1827 (1996).
19. Materials and methods are available as supporting material on Science Online.
20. M. Shepherd, J. M. Findlay, R. J. Hockey, *Q. J. Exp. Psychol. A* **38**, 475 (1986).
21. J. E. Hoffman, B. Subramaniam, *Percept. Psychophys.* **57**, 787 (1995).
22. The mean normalized thresholds (\pm SEM) for the three nontarget locations were 1.03 ± 0.05 , 1.02 ± 0.06 , and 0.95 ± 0.03 for monkey B and 1.01 ± 0.08 , 1.04 ± 0.08 , and 0.95 ± 0.06 for monkey I.
23. The mean asymptotic performances (\pm SEM) at and away from the saccade goal were $90.7 \pm 1.2\%$ and $90.0 \pm 1.2\%$ for monkey I and $94.2 \pm 0.7\%$ and $93.0 \pm 0.7\%$ for monkey B. The mean slopes (\pm SEM) at and away from the saccade goal were 2.37 ± 0.43 and 2.34 ± 0.32 for monkey I and 2.22 ± 0.34 and 2.59 ± 0.28 for monkey B.
24. K. Nakayama, M. Mackeben, *Vision Res.* **29**, 1631 (1989).
25. S. Yantis, J. Jonides, *J. Exp. Psychol. Hum. Percept. Perform.* **22**, 1505 (1996).
26. J. S. Joseph, L. M. Optican, *Percept. Psychophys.* **58**, 651 (1996).
27. M. Pare, R. H. Wurtz, *J. Neurophysiol.* **85**, 2545 (2001).
28. S. Ferraina, M. Pare, R. H. Wurtz, *J. Neurophysiol.* **87**, 845 (2002).
29. M. C. Bushnell, M. E. Goldberg, D. L. Robinson, *J. Neurophysiol.* **46**, 755 (1981).
30. E. P. Cook, J. H. Maunsell, *J. Neurosci.* **22**, 1994 (2002).
31. D. LaBerge, R. L. Carlson, J. K. Williams, B. G. Bunney, *J. Exp. Psychol. Hum. Percept. Perform.* **23**, 1380 (1997).
32. C. E. Connor, D. C. Preddie, J. L. Gallant, D. C. Van Essen, *J. Neurosci.* **17**, 3201 (1997).
33. A. Murthy, K. G. Thompson, J. D. Schall, *J. Neurophysiol.* **86**, 2634 (2001).
34. T. Sato, A. Murthy, K. G. Thompson, J. D. Schall, *Neuron* **30**, 583 (2001).
35. M. A. Basso, R. H. Wurtz, *J. Neurosci.* **18**, 7519 (1998).
36. R. Desimone, J. Duncan, *Annu. Rev. Neurosci.* **18**, 193 (1995).
37. S. Yantis *et al.*, *Nature Neurosci.* **5**, 995 (2002).
38. L. H. Snyder, A. P. Batista, R. A. Andersen, *Nature* **386**, 167 (1997).
39. L. H. Snyder, A. P. Batista, R. A. Andersen, *J. Neurophysiol.* **79**, 2814 (1998).
40. M. L. Platt, P. W. Glimcher, *J. Neurophysiol.* **78**, 157 (1997).
41. P. Mazzoni, R. M. Bracewell, S. Barash, R. A. Andersen, *J. Neurophysiol.* **76**, 1439 (1996).
42. R. M. Bracewell, P. Mazzoni, S. Barash, R. A. Andersen, *J. Neurophysiol.* **76**, 1457 (1996).
43. R. A. Andersen, C. A. Buneo, *Annu. Rev. Neurosci.* **25**, 189 (2002).
44. B. Pesaran, J. S. Pezaris, M. Sahani, P. P. Mitra, R. A. Andersen, *Nature Neurosci.* **5**, 805 (2002).
45. R. A. Andersen, C. Asanuma, G. Essick, R. M. Siegel, *J. Comp. Neurol.* **296**, 65 (1990).
46. A. L. Yarbus, *Eye Movements and Vision* (Plenum, New York, 1967).
47. We are grateful to the staff of the Laboratory of Sensorimotor Research for assistance in all aspects of this study; J. Raber and G. Tansey for veterinary care; N. Nichols and T. Ruffner for machining; J. McClurkin for help with graphics programming; L. Jensen for electronics; A. Hays for systems programming; C. Rishell and M. Szarowicz for animal care; R. Desimone for comments on a previous version of the manuscript; and M. Smith, J. Steinberg, and B. Harvey for facilitating everything. Supported by the National Eye Institute, the W. M. Keck Foundation, and the Human Frontiers Science Program.

Supporting Online Material

www.sciencemag.org/cgi/content/full/299/5603/81/DC1
 Materials and Methods
 Supporting Text
 Figs. S1 and S2
 References and Notes

15 August 2002; accepted 23 October 2002

REPORTS

Dependence of Upper Critical Field and Pairing Strength on Doping in Cuprates

Yayu Wang,¹ S. Ono,² Y. Onose,³ G. Gu,⁴ Yoichi Ando,² Y. Tokura,^{3,5} S. Uchida,⁶ N. P. Ong^{1*}

We have determined the upper critical field H_{c2} as a function of hole concentration in bismuth-based cuprates by measuring the voltage induced by vortex flow in a driving temperature gradient (the Nernst effect), in magnetic fields up to 45 tesla. We found that H_{c2} decreased steeply as doping increased, in both single and bilayer cuprates. This relationship implies that the Cooper pairing potential displays a trend opposite to that of the superfluid density versus doping. The coherence length of the pairs ξ_0 closely tracks the gap measured by photoemission. We discuss implications for understanding the doping dependence of the critical temperature T_{c0} .

The superconducting state in a metal is completely suppressed if a sufficiently strong magnetic field is applied. In individual type-II superconductors, the field required—defined as the upper critical field H_{c2} —is an important parameter because it determines the value of the coherence length ξ_0 (the size of the Cooper pair) as well as the strength of the pairing potential; the higher the field H_{c2} ,

the stronger is the pairing potential and the smaller the pair size (l). In the phase diagram of the cuprates, superconductivity has been observed in the range of hole concentration $0.05 < x < 0.25$. Many parameters of the superconducting state, notably the superfluid density and superconducting gap, have been measured as a function of x . The conspicuous exception is H_{c2} , which is uncertain for rea-

sons discussed below. Because even the basic trend of H_{c2} versus x is unknown, the crucial question of whether the pairing strength, as distinct from the superfluid density, increases or decreases with x remains unanswered. We report measurements of H_{c2} versus x in the Bi-based cuprates using the vortex-Nernst effect. In both single and bilayer systems, it was found that H_{c2} (and hence the pairing potential) steeply decreased as x increased. We show that ξ_0 is intimately related to the gap measured by angle-resolved photoemission spectroscopy (ARPES) (2) and results from scanning tunneling microscopy (STM) (3, 4).

In the Nernst effect (5–11), vortices in the vortex liquid state are driven down an applied temperature gradient $-\nabla T \parallel x$. Their velocity v

¹Department of Physics, Princeton University, Princeton, NJ 08544, USA. ²Central Research Institute of Electric Power Industry, Komae, Tokyo 201–8511, Japan. ³Spin Superstructure Project, Japan Science and Technology, Tsukuba 305–8562, Japan. ⁴Physics Department, Brookhaven National Laboratory, Upton, NY 11973, USA. ⁵Department of Applied Physics, ⁶School of Frontier Sciences, University of Tokyo, Tokyo 113–8656, Japan.

*To whom correspondence should be addressed. E-mail: npo@princeton.edu

induces an electric field $E_y = Bv_x$ which may be detected with high sensitivity (the induction field $B \parallel z$). The total Nernst signal $e_y^{\text{obs}} = E_y/|VT|$ is the sum of the vortex signal e_y and the carrier contribution e_y^N : $e_y^{\text{obs}} = e_y + e_y^N$.

Although our focus is on the Bi-based cuprates, we gain perspective and insight by first looking at the electron-doped cuprate $\text{Nd}_{2-x}\text{Ce}_x\text{CuO}_4$ (NCCO), in which the effects of fluctuations are weak and superconductivity is easily suppressed in fields of ~ 10 T. Previous Nernst measurements have revealed a sizable carrier signal e_y^N in NCCO (10, 11). We observed that e_y has a distinctive “tent” profile that distinguishes it from e_y^N (fig. S1). The vortex signal e_y at fixed T was initially zero until H exceeded the solid-to-liquid melting field $H_m(T)$ (Fig. 1A). In the liquid state, the vortex signal rises steeply to a maximum before falling monotonically to zero as H approaches H_{c2} , with a similar profile occurring in low-critical T (low- T_c) superconductors (7, 8). The steep rise just above H_m , which scales accurately with the in-plane resistivity ρ (dashed line), reflects the sharp increase in vortex mobility, whereas the fall at higher fields is caused by the field suppression of the condensate amplitude as H approaches H_{c2} . The phase diagram in Fig. 1B, derived from e_y , reveals an H_{c2} boundary similar to that observed in conventional type-II superconductors and well described by the Bardeen, Cooper, and Schrieffer (BCS) theory

(1). It is weakly T -dependent at low T and decreases to zero linearly as T approaches T_{c0} , the zero-field transition temperature [the linear H_{c2} near T_{c0} agrees with that in an earlier Nernst study (11)]. The vortex signal e_y rapidly vanishes above $T_{c0} = 24.5$ K, indicating that the amplitude of the order parameter Ψ vanishes at T_{c0} . Hence, the phase diagram of NCCO is similar to the phase diagram of conventional superconductors (1), except that the vortex liquid region is greatly expanded. This example shows that H_{c2} at finite T is reliably determined as the field at which the vortex-Nernst signal reaches zero: The tent profile of e_y versus H (a sharp rise to a peak and a fall to zero at high fields) defines the entire vortex liquid region, in which $|\Psi|$ remains finite. From $H_{c2}(0) \sim 10$ T, we find $\xi_0 \sim 58$ Å in NCCO.

Most attempts to find H_{c2} in cuprates have relied on measuring the field profiles of the resistivity ρ in intense fields. We next show that this method is highly unreliable. The field profile of ρ at 14 K (Fig. 1A, dashed line) reveals that, above H_m , it rises steeply toward the normal-state value ρ_N . Long before the field reaches H_{c2} , ρ in the vortex-liquid state becomes indistinguishable from ρ_N . If we had used the “knee” in the profile of ρ to estimate H_{c2} , we would have erroneously identified H_{c2} with the “ridge field” $H^*(T)$ defined (7) by the maximum in e_y at each T . As shown in Fig. 1B, the ridge field $H^*(T)$ versus T has a positive curvature and remains strongly T -dependent as T approaches zero. We note that many H_{c2} curves derived from ρ in cuprates share these features of $H^*(T)$ (12–14). The inset shows that at finite T , the true $H_{c2}(T)$ is considerably higher than $H^*(T)$. In the hole-doped cuprates, the difference between H^* and H_{c2} is even greater (7).

With this caveat in mind, we turn to the single-layer cuprate Bi 2201 ($\text{Bi}_2\text{Sr}_{2-y}\text{La}_y\text{CuO}_6$)

and the bilayer Bi 2212 ($\text{Bi}_2\text{Sr}_2\text{CaCu}_2\text{O}_8$), which are ideal for exploring the x dependence of H_{c2} because e_y^N is negligibly small, and the anomalously small $H_m(T)$ values allow the scaling studies described below to be extended over the broadest field range. In Bi 2201 (sample A1, $x = 0.16$, $T_{c0} = 28$ K), e_y increases to a broad maximum and then decreases monotonically to zero at just above 45 T (fig. S2). The tent profile, similar to that in NCCO except for the higher field scales, again reveals how far the vortex liquid extends in the field.

A major difference between NCCO and the hole-doped cuprates arises from strong fluctuations in the phase of Ψ in the latter. Whereas the vortex signal in NCCO rapidly vanishes just above T_{c0} , it remains large at T_{c0} in Bi 2201, $\text{La}_{2-x}\text{Sr}_x\text{CuO}_4$, and $\text{YBa}_2\text{Cu}_3\text{O}_y$ (YBCO) and extends considerably above T_{c0} . In all hole-doped cuprates examined to date (5–7, 9), T_{c0} has corresponded to the loss of long-range phase coherence (15–17), rather than the vanishing of $|\Psi|$. Defining the field at which e_y approaches zero as $H_{c2}(T)$ at each T , we found that $H_{c2}(T)$ in Bi 2201 is nearly T -independent from 5 to 30 K (it goes to zero only at much higher T). Despite the non-BCS scenario in hole-doped cuprates, $H_{c2}(T)$ is still reliably obtained from the approach of e_y to zero.

Comparison of e_y versus H in several samples of Bi 2212 of different x revealed a distinctive trend. Figure 2, A and B, compares the e_y - H curves in overdoped Bi 2212 (sample B1, $x = 0.22$, $T_{c0} = 65$ K) with those in underdoped Bi 2212 (sample B3, $x = 0.087$, $T_{c0} = 50$ K). The calibration of x is discussed in (18). In sample B1 (Fig. 2A), the vortex Nernst signal closely resembled those in Bi 2201 and anticipated the scaling property to be described. In the underdoped sample (Fig. 2B), however, the curves

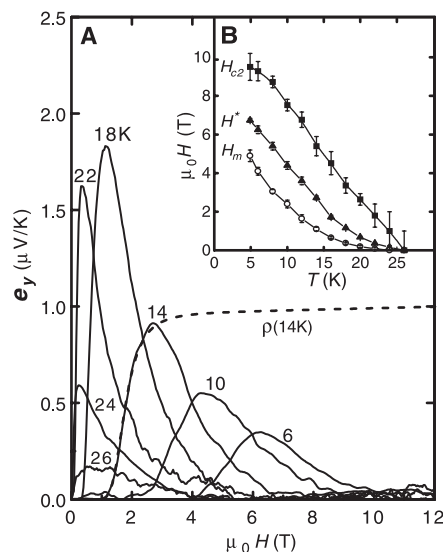


Fig. 1. (A) The vortex-Nernst signal e_y versus H in $\text{Nd}_{2-x}\text{Ce}_x\text{CuO}_4$ ($x = 0.15$, $T_{c0} = 24.5$ K). For example, at 14 K, e_y appears at $H_m = 1.1$ T, rises to a peak at $H^* = 2.8$ T, and decreases, with $H_{c2} \sim 5.8$ T. The profile of ρ at 14 K (dashed line) matches the initial increase in e_y . Above T_{c0} , the vortex signal rapidly vanishes (unlike in hole-doped cuprates). μ_0 is the vacuum permeability. (B) The T dependence of H_m , H^* , and H_{c2} derived from the e_y curves. The H_{c2} curve in NCCO is conventional and terminates close to T_{c0} .

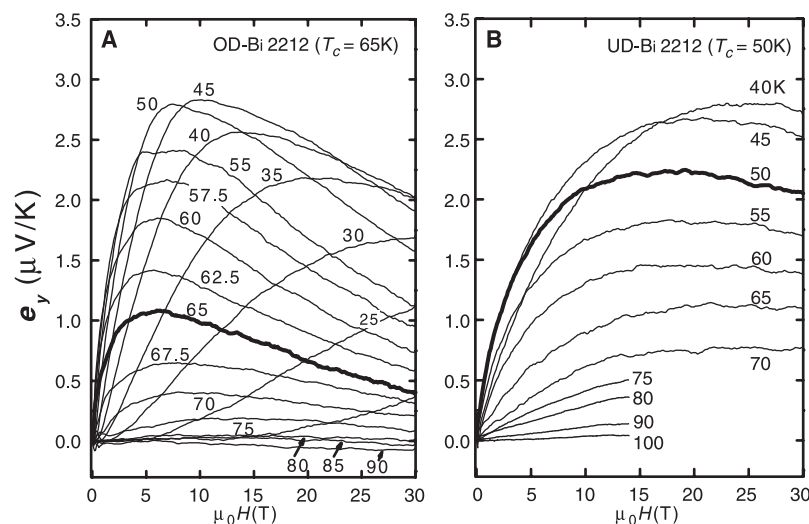


Fig. 2. Comparison of the profiles of e_y in (A) overdoped (OD) ($T_{c0} = 65$ K) and (B) underdoped (UD) ($T_{c0} = 50$ K) crystals of $\text{Bi}_2\text{Sr}_2\text{CaCu}_2\text{O}_8$. The curves in (A) peak at relatively low fields (5 to 10 T) and decrease by 50 to 60% when H reaches 30 T. The peaks in (B), however, lie much closer to 30 T.

REPORTS

were more stretched out along the field axis. In the temperature range of 40 to 50 K, e_y was not appreciably diminished from its peak value at the maximum field 30 T, whereas in Fig. 2A e_y had decreased from its peak by more than 60% by 30 T. The trend is summarized (Fig. 3A) for overdoped, optimally doped, and underdoped Bi 2212 (samples B1 to B3), using profiles of e_y measured at their respective T_{c0} 's (65, 90, and 50 K in B1, B2, and B3, respectively). It is apparent that successively higher fields are needed to achieve comparable suppression of e_y , as we go from the overdoped to the optimum and to the underdoped sample. The same pattern is observed in Bi 2201 (with lower field data).

We found that, if we used the reduced field $h = H/H_{c2}'$ as abscissa (the prime indicates the value at T_{c0}), the three traces in Fig.

3A accurately matched the template curve (18) of sample A1 (at $T_{c0} = 28$ K) with the right choice of H_{c2}' (Fig. 3B). Using the known H_{c2}' value in A1 (50 T), we found that $H_{c2}' = 50, 67,$ and 144 T in B1, B2, and B3, respectively. A similar scaling was observed in three samples of Bi 2201 (Fig. 3C). The scaling behavior enabled us to accurately track the x dependence of H_{c2}' to field values considerably higher than 45 T.

The scaling behavior continued to hold at T below T_{c0} , if comparisons were made between curves at the same reduced temperature $t = T/T_{c0}$. However, below $t \sim 0.7$, the vortex solid phase below H_m (where $e_y = 0$) expanded considerably and precluded meaningful comparison for scaling behavior. This was not a serious drawback because the T

dependence of H_{c2} was very weak between 0 K and T_{c0} in the Bi-based cuprates (the prime on H_{c2}' is dropped hereafter).

We carried out the scaling comparison for five samples of Bi 2212 with $0.087 < x < 0.22$, as well as in three samples of Bi 2201, and obtained the variation of H_{c2} versus x displayed (Fig. 4A). As the doping x decreases, H_{c2} in Bi 2212 undergoes a steep increase from 50 to 144 T, whereas in Bi 2201 it increases from 42 to 65 T. The gap amplitude Δ_0 in Bi 2212, measured at low T by ARPES (2), also increases as x decreases (Fig. 4A, upper stripe). Most investigators regard this increasing Δ_0 as the normal-state gap in the pseudogap state because it persists unchanged in size (2) to temperatures well above T_{c0} .

We next show that our values for H_{c2} in Bi 2212 are in fact closely related to Δ_0 . The two quantities may be compared directly if we convert them to length scales. Expressing H_{c2} as the coherence length via $\xi_0 = \sqrt{(\phi_0/2\pi H_{c2})}$, we found that ξ_0 decreases from 26 to 15 Å as x decreases from 0.22 to 0.087 (ϕ_0 is the flux quantum). The gap Δ_0 may be converted to the Pippard length by $\xi_P = \hbar v_F/a\Delta_0$, where $v_F = 1.78 \times 10^5$ m/s is the Fermi velocity ($a = \pi$ for s -wave superconductors). The plots in Fig. 4B reveal that ξ_0 and ξ_P are closely matched if we choose $a = 3/2$, consistent with extreme gap anisotropy. The agreement is strong evidence that the ARPES gap at low T and the Nernst experiments are probing the same length scale over a broad range of x . Both experiments uncovered the same trend: The coherence length decreases by a factor of ~ 2 as x decreases from 0.22 to 0.087. Moreover, the virtually T -independent behavior of H_{c2} in our experiment is consistent with the T -independent behavior in the ARPES gap. The comparison persuaded us that the ARPES Δ_0 (2) represents the gap amplitude of the Cooper pairs.

High-resolution images of vortices in optimally doped Bi 2212 have been obtained by STM. The exponential decay of the quasiparticle state density yields a length scale of 22 Å (3). A longer length scale, ~ 40 Å, is defined by the checkerboard pattern imaged outside the core (4). The shorter length of 22 Å is in good agreement with our ξ_0 (Fig. 4B, open triangle), suggesting that the exponential fall-off is dictated by ξ_0 .

Recently, the field scale H_{pg} for suppressing the pseudogap state in Bi 2212 has been estimated from the c -axis resistivity ρ_c versus H (19). Insofar as ρ_c probes changes in the single-particle density of states, rather than the pairing amplitude, the inferred H_{pg} values should be distinguished from H_{c2} (indeed, the estimated H_{pg} values, 100 to 550 T, are much higher than our H_{c2} values).

To address our initial question, the present experiment establishes that H_{c2} increases as x decreases in both Bi 2201 and Bi 2212, which

Fig. 3. (A) The curves of e_y versus H in overdoped (sample B1), optimally doped (OPT) (sample B2), and underdoped (sample B3) Bi 2212 taken at their T_{c0} 's (65, 90, and 50 K, respectively). (B) The collapse of the three curves in (A) onto the template curve from Bi 2201 (sample A1 with $T_{c0} = 28$ K) when plotted against $h = H/H_{c2}'$. (C) Comparison of the scaled profiles of e_y versus h in two other samples of Bi 2201 (measured up to 14 T) against the template curve in sample A1.

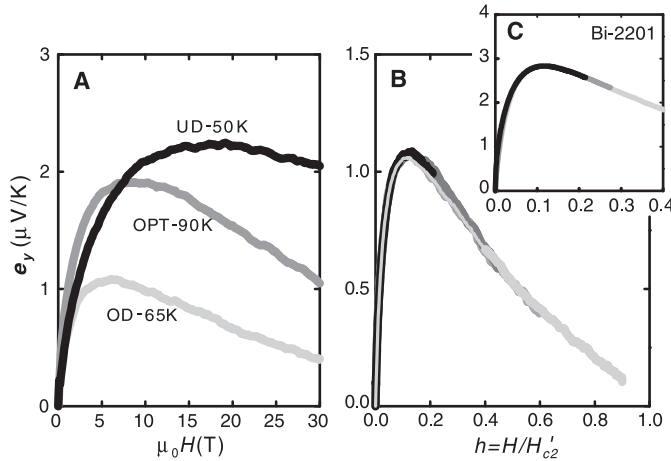
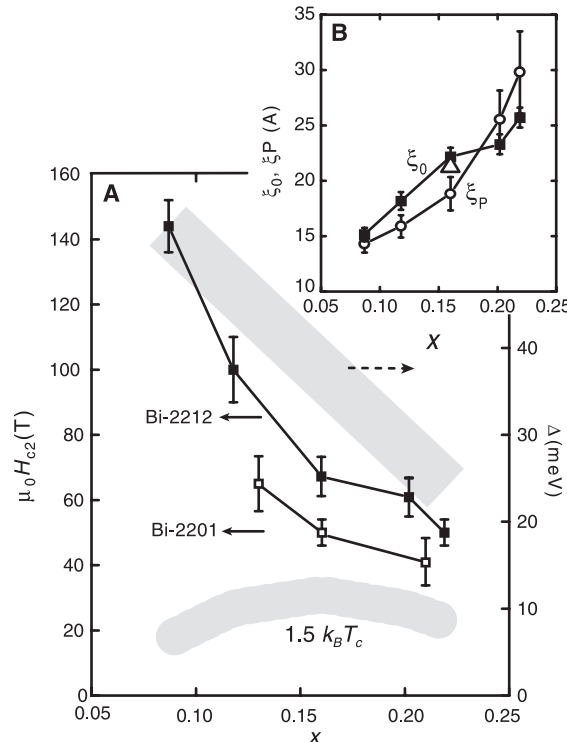


Fig. 4. (A) The x dependence of H_{c2} in Bi 2212 (solid squares) and in Bi 2201 (open squares) measured by scaling of Nernst profiles. As indicated, the upper gray stripe is the x dependence of the ARPES gap Δ_0 (2) and the lower gray stripe is T_{c0} . (B) Comparison of the coherence length ξ_0 (solid squares) obtained from H_{c2} and the Pippard length ξ_P (open circles) obtained from Δ_0 . The decay length of quasiparticle states imaged by STM (3) is shown as an open triangle.



implies that the pairing potential is strongest in very underdoped samples. This finding may place strong constraints on theories of the pairing mechanism. The trend [opposite to that of the superfluid density n_s (20, 21), which decreases as x decreases] implies a scenario for underdoped cuprates that is radically different from that inferred from n_s and T_{c0} alone. The physical picture is that, in hole-doped cuprates, the pairing potential Δ_0 is maximal in the underdoped regime and falls rapidly with increased hole density, as anticipated in early resonating-valence-bond theories (15, 16). However, the small n_s at small x renders the condensate highly susceptible to phase fluctuations (17). At T_{c0} , spontaneous nucleation of highly mobile vortices destroys long-range phase coherence and the Meissner state (7, 22, 23), but vortex excitations remain observable to much higher T (5, 6). As x is increased, n_s and T_{c0} initially increase, but beyond $x = 0.17$, T_{c0} is suppressed by a steeply falling Δ_0 . The trade-off between n_s and Δ_0 informs the entire cuprate phase diagram and accounts naturally for the dome shape of the curve of T_{c0} versus x .

An interesting implication may be inferred in the limit of small x . If the trend in ξ_0 in Fig. 4B persists, ξ_0 becomes smaller than the separation d of Cooper pairs in this limit ($d \sim 25 \text{ \AA}$ at $x = 0.05$). For $x < 0.05$, we may treat the carriers as tightly bound pairs (bosons) that are well separated and too dilute to sustain long-range phase coherence. In uncovering the increased pairing strength at small x , our experiment provides clues that bosonic pairs may exist in this limit.

References and Notes

1. M. Tinkham, *Introduction to Superconductivity* (McGraw-Hill, New York, ed. 2, 1996).
2. H. Ding et al., *Phys. Rev. Lett.* **87**, 227001 (2001).
3. S. H. Pan et al., *Phys. Rev. Lett.* **85**, 1536 (2000).
4. J. E. Hoffman et al., *Science* **295**, 466 (2002).
5. Z. A. Xu, N. P. Ong, Y. Wang, T. Kakeshita, S. Uchida, *Nature* **406**, 486 (2000).
6. Y. Wang et al., *Phys. Rev. B* **64**, 224519 (2001).
7. Y. Wang et al., *Phys. Rev. Lett.* **88**, 257003 (2002).
8. F. Vidal, *Phys. Rev. B* **8**, 1982 (1973).
9. C. Capan et al., *Phys. Rev. Lett.* **88**, 56601 (2002).
10. P. Fournier et al., *Phys. Rev. B* **56**, 14149 (1997).
11. F. Gollnik, M. Naito, *Phys. Rev. B* **58**, 11734 (1998).
12. A. P. Mackenzie et al., *Phys. Rev. Lett.* **71**, 1238 (1993).
13. M. S. Osofsky et al., *Phys. Rev. Lett.* **71**, 2315 (1993).
14. Y. Ando et al., *Phys. Rev. B* **60**, 12475 (1999).
15. G. Baskaran, Z. Zou, P. W. Anderson, *Solid State Commun.* **63**, 973 (1987).
16. G. Kotliar, J. Liu, *Phys. Rev. B* **38**, 5142 (1988).
17. V. J. Emery, S. A. Kivelson, *Nature* **374**, 434 (1995).
18. Materials and methods are available as supporting material on Science Online.
19. T. Shibauchi, L. Krusin-Elbaum, Ming Li, M. P. Maley, P. H. Kes, *Phys. Rev. Lett.* **86**, 5763 (2001).
20. D. A. Bonn et al., *Czech J. Phys.* **46**, 3195 (1996).
21. Y. J. Uemura et al., *Phys. Rev. Lett.* **62**, 2317 (1989).
22. Z. Tešanović, *Phys. Rev. B* **51**, 16204 (1995).
23. A. K. Nguyen, A. Sudbø, *Phys. Rev. B* **57**, 3123 (1998).
24. We thank S. Hannahs for help with measurements at the National High Magnetic Field Laboratory, Tallahassee, FL, a facility supported by NSF and the

state of Florida. N.P.O., S.U. and Y.T. are supported by a grant from the New Energy and Industrial Technology Development Organization, NEDO (Japan). N.P.O. acknowledges support from NSF (grant NSF-DMR 98-09483) and the U.S. Office of Naval Research (contract N00014-01-0281). G.G. acknowledges support from the U.S. Department of Energy (contract DE-AC02-8CH10886).

Supporting Online Material

www.sciencemag.org/cgi/content/full/299/5603/86/DC1
Materials and Methods
Figs. S1 and S2
References

13 September 2002; accepted 15 November 2002

Three-Dimensional Mapping of Dislocation Avalanches: Clustering and Space/Time Coupling

Jérôme Weiss¹ and David Marsan²

There is growing evidence for the complex, intermittent, and heterogeneous character of plastic flow. Here we report a three-dimensional mapping of dislocation avalanches during creep deformation of an ice crystal, from a multiple-transducers acoustic emission analysis. Correlation analysis shows that dislocation avalanches are spatially clustered according to a fractal pattern and that the closer in time two avalanches are, the larger the probability is that they will be closer in space. Such a space/time coupling may contribute to the self-organization of the avalanches into a clustered pattern.

Dislocation-driven plastic deformation has been described as a smooth flow process that is homogeneous in both space and time, yet there is evidence for the intermittent and heterogeneous character of plastic flow (1). The spontaneous formation of fractal dislocation cell patterns has been reported in metals (2, 3), and scale-invariant patterning of dislocation arrays was also obtained in numerical simulations (4). These observations, however, provide a static characterization of the spatial heterogeneity of dislocation patterns after deformation. Surface observations in metals indicate that slip consists of intermittent events localized along slip bands (1), and the temporal heterogeneity of slip has been extensively explored in the Portevin-Le Chatelier effect (5). Recently, acoustic emission (AE) studies performed during the creep of single ice crystals, coupled with numerical simulations of collective dislocation motion, revealed a strongly intermittent plastic flow characterized by jerks of dislocations with power law distributions of energies $P(E) \sim E^{-\tau}$ (6–8) where $P(E)$ is the probability density function of the energy E . This feature is shared by other slowly driven systems (9), including fracture in disordered materials (10, 11). These dislocation avalanches are also clustered in time (12). In these experiments, complexity and multiscale properties arose solely from dislocations interacting via long-range internal stresses (decreasing with the distance r as $1/r$).

The evidence for heterogeneity and scale

invariance in space, time, and energy calls for the development of new models of dislocation systems and plastic flow (13) and for a nonequilibrium statistical theory of dislocation motion (7). Yet, to further constrain theoretical development, a complete dynamical picture of plastic flow simultaneously in space, time, and energy domains is still lacking. Here we present three-dimensional (3D) mapping of dislocation avalanches during viscoplastic deformation of a crystalline material. The experiment, performed on a single crystal of ice Ih, was similar to those performed previously (7, 12), except that we used multiple transducers to map the hypocenters of the microseismic waves generated by the sudden local displacements associated with the dislocation avalanches. Compression creep (constant load) was applied to a cylindrical crystal under stress and temperature conditions in which diffusional creep is not a significant mechanism of inelastic deformation. Ice is an ideal material in which to explore collective dislocation dynamics with AE measurements: It deforms by dislocation slip even at temperatures close to the melting point; its transparency allows microcracking to be ruled out as a source of AE; and the transducers can be frozen on the specimen, yielding optimum acoustic coupling (6, 7, 14). The basal planes, which are the preferred slip planes in hexagonal ice, were inclined at the beginning of the test to 11° from the compression axis. A classical macroscopic creep behavior was observed, with primary and secondary creep followed by a roughly exponential growth of the strain rate during tertiary creep. Here, tertiary creep did not result from microcracking but from a rapid multiplication of dislocations. Because acoustic activity is a proxy of global deformation (14), most of the

¹Laboratoire de Glaciologie et Géophysique de l'Environnement-CNRS, 54 rue Molière, BP 96, 38402 St. Martin d'Hères Cedex, France. ²Laboratoire de Géophysique Interne et Tectonophysique, Université de Savoie, 73376 Le Bourget du Lac Cedex, France.